Article:
Ahmed, M., Nair, A., Middleton, J. et al. (2026) Enhancing mRNA therapeutics production: A platform technology approach through IVT modeling insights. Results in Engineering, 30. 110088. ISSN: 2590-1230

https://doi.org/10.1016/j.rineng.2026.110088

Results in Engineering 30 (2026) 110088

Contents lists available at ScienceDirect

Results in Engineering

journal homepage: www.sciencedirect.com/journal/results-in-engineering

Research paper

Enhancing mRNA therapeutics production: A platform technology approach through IVT modeling insights

Mahdi Ahmed, Aditya Nair, Joseph Middleton, Kate Loveday, Solomon Brown, Zoltan Kis, Joan Cordiner *

School of Chemical, Materials and Biological Engineering, University Of Sheffield Mappin Street, S1 3JD, Sheffield, United Kingdom

ARTICLE INFO

Keywords:
mRNA production
IVT process optimization
Bio-process modeling

ABSTRACT

Rapid, scalable production of high-quality mRNA underpins vaccines, gene therapies, and protein replacement medicines, yet optimisation of the in vitro transcription (IVT) step is often driven by template-specific trial-and-error. We present a first-principles mechanistic IVT bioprocess model—constructed from thermodynamic equilibria, enzyme kinetics, and stoichiometric mass balances—to support Quality-by-Design (QbD) manufacturing. The model is calibrated and validated against > 100 experiments from a Latin Hypercube design that varies nucleotide triphosphate (NTP) concentration, magnesium concentration, T7 RNA polymerase loading, template DNA, spermidine, and reaction time, using two contrasting templates: a SARS-CoV-2 spike construct (CSP) and enhanced green fluorescent protein (eGFP). The model predicts RNA yield with R^2 = 0.85–0.87 while explicitly tracking individual NTP consumption and magnesium pyrophosphate precipitation. Within a QbD context, the framework links critical process parameters (CPPs) and critical material attributes (CMAs) to product-oriented metrics and manufacturing key performance indicators (KPIs), and identifies a model-derived operating window that reduces reagent cost subject to specified quality constraints. Mechanistic refinements, including inorganic pyrophosphatase kinetics and sequence-aware per-base NTP accounting, support transfer between the two templates studied here and provide a foundation for broader multi-construct validation. Overall, the approach offers a data-efficient route to accelerate IVT process development and reduce consumable spend for emerging mRNA therapeutics.

1. Introduction

The COVID-19 pandemic has demonstrated the need for the rapid development of medical interventions against emerging infectious diseases. Traditional vaccine development methods are constrained by slow production cycles and limited adaptability, proving ineffective in responding to fast-evolving viral threats [1]. Yet, messenger RNA (mRNA)-based therapeutics avoid these limitations, and recent technological advancements have facilitated the use of mRNA as a platform technology, with both preventive and therapeutic applications against viral diseases and a variety of chronic diseases–including several forms of cancers, genetic diseases, autoimmune disorders, rare diseases, and cardiovascular diseases respectively [2,3].

This is possible thanks to the unique mechanism of action of mRNA vaccines and therapeutics, collectively referred to as *mRNA medicines*. They operate by delivering an mRNA sequence to host cells, which then produce a target protein. In principle, any protein sequence with any function can be encoded on mRNA [4]. Indeed, mRNA technology is deployed for infectious disease vaccinology and is also being developed for individualized cancer therapy, chimeric antigen receptor T-cell (CAR-T) therapy, gene therapy, gene editing, and protein replacement therapy applications. The efficacy of these vaccines and therapeutics depends on the ability to rapidly produce high-quality mRNA; therefore, the demand for robust RNA manufacturing platform processes is ever growing. Implementing Quality by Design (QbD) principles is essential in this context, as QbD provides a systematic approach to manufacturing that starts with predefined objectives and emphasizes thorough product and process understanding based on sound science and quality risk management [5]. In mRNA production, QbD links critical quality attributes (CQAs) to critical process parameters (CPPs) and critical material attributes (CMAs), including template DNA integrity/purity and polymerase activity, so that sequence-dependent quality attributes can be controlled in a platform setting. For mRNA *therapeutics*, these CQAs extend beyond bulk yield to include capping efficiency/integrity,

* Corresponding author.
E-mail addresses: smahmed3@sheffield.ac.uk (M. Ahmed), a.nair@sheffield.ac.uk (A. Nair), j.middleton5@sheffield.ac.uk (J. Middleton), k.a.loveday@sheffield.ac.uk (K. Loveday), s.f.brown@sheffield.ac.uk (S. Brown), z.kis@sheffield.ac.uk (Z. Kis), j.cordiner@sheffield.ac.uk (J. Cordiner).

https://doi.org/10.1016/j.rineng.2026.110088
Received 14 December 2025; Received in revised form 10 March 2026; Accepted 12 March 2026
Available online 17 March 2026

Nomenclature

Abbreviations

IVT	In vitro transcription
QbD	Quality by Design
CPP	Critical Process Parameter
CMA	Critical Material Attribute
CQA	Critical Quality Attribute
NTP	Nucleoside triphosphates
cGMP	Current Good Manufacturing Practice
KPI	Key Performance Indicator
LHS	Latin Hypercube Sampling
RRMSE	Relative Root Mean Square Error
RMPSE	Relative Mean Percent Square Error
CSP	SARS-CoV-2 spike
eGFP	Enhanced green fluorescent protein
AEX-HPLC	Anion-exchange chromatography
GSA	Global sensitivity analysis
DoE	Design of Experiments
DE	Differential Evolution (optimizer)
BFGS	Broyden-Fletcher-Goldfarb-Shanno (optimizer)
GC (%)	Guanine-cytosine content (percent)
nt	Nucleotides (unit of length)

Constants

K_i	Equilibrium constants for association)
k_{app}	Apparent catalytic coefficient in transcription-rate expression
k_1, k_2	Empirical inhibition coefficients in the transcription-rate denominator
k_{precip}	Effective precipitation coefficient in V_{precip}
k_{PPase}	Pyrophosphatase kinetic parameter in $V_{\text{hydrolysis}}$
k_d	First-order deactivation rate constant for T7RNAP
R	Universal gas constant
T	Temperature (K)

Species and Components

ATP, GTP, CTP, UTP	Ribonucleoside triphosphates
RNA	Product RNA
dsRNA	Double-stranded RNA
DNA	Template DNA
T7RNAP	T7 RNA polymerase
PPase	Inorganic pyrophosphatase
Mg^{2+}	Magnesium ion
PPi	Inorganic pyrophosphate
Pi, HPi	Orthophosphate species (lumped as Pi; protonated form HPi)
MgPPi	Magnesium pyrophosphate (precipitate)
Spd^{3+}	Spermidine ion (dominant charge state under IVT)
HAc, Ac^-	Acetic acid / acetate

Variables

t	Time (min)
V_{tr}	Transcription rate
V_{ann}, V_{melt}	dsRNA annealing and melting fluxes
V_{precip}	Rate of Mg-pyrophosphate precipitation
$V_{\text{hydrolysis}}$	PPi hydrolysis rate (PPase-coupled)
V_{raw}	Intrinsic (uncapped) volumetric NTP-incorporation rate
V_{max}	Rate ceiling; $\min\{V_{\text{unit}}, V_{\text{part}}\}$
V_{unit}	Unit-activity ceiling (Unit$\cdot\mu$L^{-1} to rate)
V_{part}	Polymerase-throughput ceiling
G	Geometric-mean substrate factor over {MgATP, MgCTP, MgGTP, MgUTP}
r_{RNAP}	Per-T7RNAP throughput (transcripts min^{-1} per enzyme)
E	Active T7RNAP concentration (mol L^{-1})
U	Volumetric activity of T7RNAP (Unit $\cdot\mu$L^{-1})
τ_{init}	Initiation dwell time
ℓ_{init}	Initiation segment length (nt)
v_{init}	Initiation speed (nt s^{-1})
v_{el}	Elongation speed (nt time^{-1})
N_{all}	Total nucleotides per transcript
N_a, N_g, N_c, N_u	Per-base counts in one transcript (A,G,C,U)

residual template DNA and process proteins, sequence integrity (e.g., truncations), and immunostimulatory by-products such as double-stranded RNA (dsRNA). As a result, IVT operation must be selected as a trade-off between productivity, quality proxies and reagent economy, rather than by yield alone.

As emphasized across recent reviews, the strength of the mRNA platform is its modular, largely cell-free workflow, which allows the encoded sequence to be swapped quickly while core unit operations remain similar [3]. Exploiting this flexibility at scale demands explicit control of sequence-dependent and process-dependent quality attributes (e.g., capping efficiency, poly(A) length, dsRNA, and truncations). Foundational overviews detail the platform's rapid design cycle and key sources of variability tied to RNA chemistry and delivery [2]. From a manufacturing perspective, end to end IVT workflows (template preparation → IVT and capping → purification via DNase, precipitation, chromatography/TFF → LNP formulation and fill and finish) reveal bottlenecks in yield, impurity control (notably dsRNA), and scalable analytics [3]. A Quality by Design framing links template and material choices (sequence/UTRs, modified nucleotides) and IVT parameters (polymerase type or variant, promoter and sequence context, NTP/Mg^{2+}, temperature/residence time) to critical quality attributes, enabling robust, indication-agnostic "platform" control strategies and model-based optimization [6]. Accordingly, our platform workflow links sequence- and process-level inputs to validated model predictions and then to QbD design-space and cost-aware optimization outputs under template switching. This need is most acute for personalized and rare-disease programs, where batch sizes are smaller, template switching is frequent, and extensive construct-specific DoE is often impractical. In such settings, transferable models that can propose revised operating windows with minimal new experimentation can substantially reduce development time and raw-material waste. Mechanistically, bacteriophage RNA polymerases, especially engineered T7 variants, couple promoter/template sequence to IVT productivity and byproducts, offering routes to higher yield and lower innate immunostimulation across diverse mRNA designs [7].

Moreover, RNA yield and nucleotide-triphosphate (NTP) consumption are critical key-performance indicators in mRNA manufacturing because they directly govern both process efficiency and overall cost. Control of NTP usage becomes particularly important when expensive modified nucleotides (e.g., N_1 methyl-pseudouridine triphosphate) and co-transcriptional cap analogues (such as CleanCap AG) dominate raw-material expenditure.

Mechanistic efforts to model IVT have shown promise: Berg *et al.* developed a detailed kinetic description of T7-mediated transcription, and

Stover *et al.* extended this line of work by explicitly modeling the formation of magnesium–pyrophosphate precipitate [8,9]. Both studies, however, were parameterized and validated within relatively constrained regions of the operating space using targeted experimental designs. Such limited designs can make it easy to over-fit a model to a specific region of the process space, miss higher-order parameter interactions, and provide only modest predictive power when conditions change. In parallel, Design-of-Experiments (DoE) QbD studies have mapped IVT design spaces for yield, cost and quality targets [10,11]. Notably, Boman *et al.* also showed that a DoE-derived model can retain validity when transferred between constructs of different lengths [11]; nevertheless, these approaches remain largely template- and assay-specific and do not, in general, couple kinetics, precipitation and economics in a way that is transferable across multiple mRNA sequences and robust to the high-dimensional variability now common in modern process development.

Predictive models should facilitate real-time adjustments to the manufacturing process, optimizing resource use and reducing waste through recycling. This approach helps maintain process consistency and ensures compliance with stringent regulatory standards, even across different DNA templates while minimizing by-product formation [12]. Predictive models can also lay the groundwork for future integration with advanced control strategies, supporting a more robust and responsive approach to optimizing production and ensuring the safety and efficacy of mRNA-based therapeutics.

A design space can therefore be defined in which the required product quality can be consistently achieved using QbD principles, rather than quality by testing, ensuring product efficacy and patient safety. Models can improve the performance of the manufacturing process by increasing productivity, enhancing resource efficiency, and reducing costs. By defining this design space, manufacturers can better control critical process parameters, ensuring consistent and high-quality output across various mRNA products.

In this work we develop a mechanistic IVT bioprocess model intended for platform use across diverse mRNA sequences and operating conditions. The model is calibrated and validated on a six-parameter Latin Hypercube Sampling (LHS) dataset for *two* distinct templates–SARS-CoV-2 Spike (CSP) and enhanced green fluorescent protein (eGFP)–so as to test transferability across sequence length and composition while covering a noisy multidimensional parameter space. The dataset simultaneously varies NTP concentration, Mg^{2+}, T7 RNA polymerase (T7RNAP), template DNA, spermidine, and reaction time, capturing the complex interactions that industrial process development must navigate. Building on established T7 RNA-synthesis kinetics, we integrate (i) Mg-PP_i precipitation dynamics with inorganic pyrophosphatase (PPase) effects, (ii) explicit sequence-dependent terms (template length/base composition) and template-DNA concentration, (iii) spermidine-mediated modulation of enzyme-DNA interactions, and (iv) per-base NTP accounting that links sequence composition directly to resource use. Within a QbD framework, we link CPPs and CMAs to CQAs and use the model to find an operating window that balances yield, quality and reagent economy.

This modeling strategy is designed to reduce reliance on resource-intensive traditional Design of Experiments (DoE) protocols, which are slow to adapt to new data, as noted by Gilman *et al.* [13] and Kumar *et al.* [14]. By mapping the multidimensional design space of RNA synthesis in the IVT bioreactor, we show how mechanistic insight, global sensitivity analysis and cost-aware optimization can converge to provide a transferable, platform-ready digital twin. The remainder of this paper details the theoretical foundations, experimental data, model calibration, and QbD-driven design space analysis that together provide a flexible tool for rapid, cost-effective, and scalable production of next-generation mRNA medicines.

Critically, the model is constructed entirely from mechanistic first principles—thermodynamic equilibria, enzyme kinetics, and stoichiometric mass balances—rather than being derived from experimental data. Experimental data serve exclusively as a support function: a small number of effective kinetic parameters are calibrated against a Latin Hypercube dataset, and an independent precipitation dataset provides validation. Fig. 1 summarises this bottom-up workflow.

2. Methods

2.1. Model formulation

This model extends the mechanistic framework of Akama et al. and Berg et al. by adapting their core rate expressions for T7RNAP-catalyzed transcription [8,15]. Beyond these established components, we introduce several novel modules: (i) spermidine-mediated modulation of polymerase activity, (ii) explicit template DNA concentration, length, and sequence-dependent effects, (iii) individual NTP incorporation stoichiometries and (iv) precipitation quantification across templates. Together, these additions enhance the model's accuracy and its ability to optimize RNA yield and quality across diverse mRNA templates.

Spermidine

Spermidine (predominantly Spd^{3+} under IVT conditions) screens the polyanionic phosphate backbone and promotes formation and stabilization of promoter complexes via multivalent electrostatic interactions, increasing productive initiation [16]. We assume rapid, order-agnostic association and represent the net effect with a single ternary parameter that we estimate. The binary assemblies: $[DNA^- \cdot T7RNAP]$, $[DNA^- \cdot Spd^{3+}]$, and $[T7RNAP \cdot Spd^{3+}]$ are part of the overall formulation (Appendix A). Their sequence- and salt-dependent contributions are absorbed into the ternary parameter K_{12}.

$$K_{12} = \frac{[DNA^- \cdot T7RNAP \cdot Spd^{3+}]}{[DNA^-][T7RNAP][Spd^{3+}]}. \tag{1}$$

Transcription rate with multi-substrate limitation

Tracking the consumption of individual NTPs enables more informed control of reagent usage and waste, because the demand for each NTP is sequence-dependent (via base composition) and can vary with operating conditions that affect reaction rate and yield.

Elongation by T7RNAP proceeds by adding one MgNTP per incorporation step, determined by the template base at the active site. Although each step depends only on the matching nucleotide, completion of a full-length transcript requires availability of all four NTPs by stoichiometry; therefore, as any required NTP approaches depletion, the net transcript completion rate must decrease and ultimately tends to zero, particularly when one species is consumed faster than the others.

$$V_{tr} = k_{app}\,[DNAT7RNAPSpd]\,[Mg]\,\frac{\mathcal{G}([MgATP], \ldots, [MgUTP])}{1 + k_1[Mg] + k_2 \sum_i [MgNTP_i]} \tag{2}$$

$$\mathcal{G} = \left(\frac{[MgATP]}{N_a} \frac{[MgCTP]}{N_c} \frac{[MgGTP]}{N_g} \frac{[MgUTP]}{N_u} \right)^{1/4}, \tag{3}$$

The total nucleotide count per full transcript is

$$N_{all} = N_a + N_g + N_c + N_u$$

where N_i represents the number of *moles* of nucleotide i ($i = a, g, c, u$) consumed per mole of product RNA.

The geometric-mean term $\mathcal{G}$ is used to provide a smooth multi-substrate limitation with the correct limiting behaviour. When all $[MgNTP_i]$ are sufficiently high, the transcription rate approaches an effectively non-limiting (single-substrate) form. Conversely, as any $[MgNTP_i]$ becomes limiting relative to the others, $\mathcal{G}$ scales with that species, giving an approximately first-order dependence on the most-depleted nucleotide and smoothly driving V_{tr} toward zero without discontinuities. For parsimony, we apply identical equilibrium constants across the four NTP species; nucleotide-specific binding differences are not identifiable from the available data and are therefore absorbed into the effective fitted kinetic parameters.

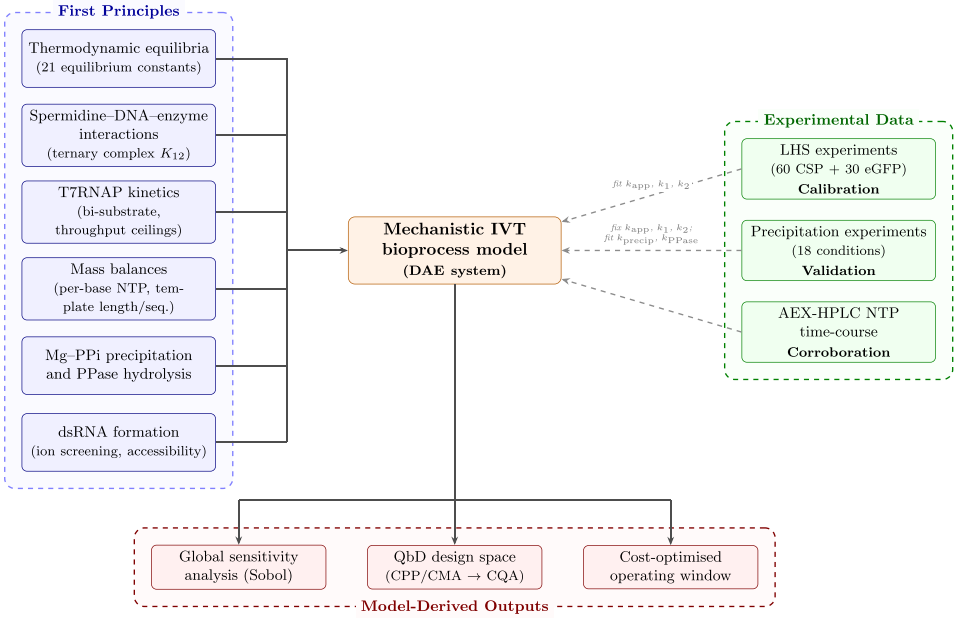

Fig. 1. Bottom-up modelling workflow. The mechanistic IVT model (centre) is assembled from first-principles components (left), including thermodynamic equilibria, spermidine–DNA–enzyme interactions, T7RNAP kinetics with throughput ceilings, per-base mass balances with template-specific stoichiometry, Mg–PPi precipitation, and dsRNA formation. Experimental data (right, dashed arrows) serve only to calibrate three effective kinetic parameters (k_{app}, k_1, k_2) against an LHS dataset; these are then held fixed while k_{precip} and k_{PPase} are fitted to an independent precipitation dataset. An AEX-HPLC NTP time-course provides additional independent check. The validated model generates QbD outputs (bottom) including global sensitivity analysis, design-space mapping, and cost-optimised operating windows.

Throughput ceiling

The total nucleotide count per transcript N_{all} (nt) enters the *throughput ceilings* by converting an NTP-incorporation capacity into an equivalent transcript-flux capacity (mol RNA L^{-1} $time^{-1}$); it does not by itself change the intrinsic initiation/elongation kinetics. Accordingly, we cap the intrinsic transcript synthesis flux by

$$V_{max} = \min\{ V_{unit}, V_{part} \}, \qquad V_{tr} = \min\{ V_{raw}, V_{max} \}, \tag{4}$$

where V_{raw} is the intrinsic (uncapped) volumetric transcript synthesis rate (mol RNA L^{-1} $time^{-1}$). By the conventional Unit definition (one Unit incorporates 1 nmol of NTP in 60 min at 37°C), a volumetric activity U (Unit μL^{-1}) corresponds to an NTP-incorporation capacity of $U\,(1\,\text{nmol}/60\,\text{min})\,(10^{-9}\ \text{mol nmol}^{-1})\,(10^{6}\ \mu L\,L^{-1})$; expressed as a transcript-flux ceiling, this gives

$$V_{unit} = \frac{U\,(1\,\text{nmol}/60\,\text{min})\,(10^{-9}\ \text{mol nmol}^{-1})\,(10^{6}\ \mu L\,L^{-1})}{N_{all}}. \tag{5}$$

The polymerase–throughput ceiling depends on the active enzyme concentration E (mol L^{-1}) and the per-RNAP throughput r_{RNAP}; with $\tau_{init} = \ell_{init}/v_{init}$,

$$r_{RNAP} = \min\left\{ \frac{1}{\tau_{init}}, \frac{v_{el}}{N_{all}} \right\}, \tag{6}$$

$$V_{part} = E\, r_{RNAP}, \qquad E = \frac{U\,(10^{6}\ \mu L\,L^{-1})}{S_{mol}}. \tag{7}$$

Here ℓ_{init} (nt), v_{init} and v_{el} (nt $time^{-1}$) summarize initiation/elongation kinetics; S_{mol} (Unit $\cdot mol^{-1}$) is the supplier's specific activity used to convert Units to moles of active enzyme. The factor $(10^{6}\ \mu L\,L^{-1})$ converts quantities expressed per μL to a per-L basis. These ceilings tighten as N_{all} increases in the elongation-limited regime ($r_{RNAP} \approx v_{el}/N_{all}$); however, when initiation/termination dominates ($r_{RNAP} \approx 1/\tau_{init}$), transcript length has little impact on the effective rate. We use these ceilings to set weakly informative bounds on fitted kinetic constants (see Appendix B).

Precipitation

We refer to orthophosphate collectively as Pi and treat its protonation states via the acid–base speciation in Appendix A. Under excess pyrophosphatase, pyrophosphate is converted to two Pi.

$$\text{PPi} + \text{H}_2\text{O} \longrightarrow 2\,\text{HPi}. \tag{8}$$

Precipitation typically requires supersaturation and exhibits an induction (time/concentration) delay; with endpoint-only data we do not resolve this dynamically and instead lump it into a single effective coefficient:

$$V_{precip} = k_{precip}\,[\text{PPi}]_{free}, \tag{9}$$

$$V_{hydrolysis} = \frac{[\text{PPi}]_{free}\,[\text{PPase}]}{k_{PPase} + [\text{PPi}]_{free}}. \tag{10}$$

Eq. (10) couples pyrophosphate hydrolysis to PPase activity; if hydrolysis is insufficient, PPi accumulates, complexes with Mg^{2+}, and would precipitate irreversibly [17]. Eq. (15) tracks this hydrolysis as PPi is hydrolyzed into twice as many Pi.

k_{precip} is a lumped parameter that captures supersaturation-driven onset and induction over the batch; this is identifiable from endpoint experimental data. If precipitation is negligible under a given condition (PPase in excess), set $V_{precip} = 0$.

Magnesium–acetate

Because magnesium is supplied as the acetate salt, we include the acetate conjugate pair (HAc/Ac^-) and weak Mg-acetate complexation ($[MgAc]^+$, $[MgAc_2]$). We track only solution-phase magnesium here; any precipitated magnesium pyrophosphate is handled as a separate solid pool.

$$Mg_{tot}^{(sol)} = [Mg^{2+}] + \sum_i [\text{MgNTP}_i] + [\text{MgAc}]^+ + [\text{MgAc}_2] + \ldots \tag{11}$$

$$\text{Ac}_{tot} = [\text{Ac}^-] + [\text{HAc}] + [\text{MgAc}]^+ + 2[\text{MgAc}_2], \tag{12}$$

At pH 7-8, acetate provides only minor buffering relative to the primary buffer, but including Eqs. (11)-(12) yields a realistic free $[Mg^{2+}]$ and, by extension, Mg-NTP availability.

Differential equations

The ordinary differential equations (ODEs) governing the system are shown in Eqs. (13)-(24). All novel kinetic terms appear here in this system. Kinetic terms relating to dsRNA formation are shown in Appendix C. No degraded mRNA was observed in the experiments, so all terms relating to degradation from previous models are neglected here.

$$\frac{d[\text{RNA}]}{dt} = V_{\text{tr}} - 2V_{\text{ann}} + 2V_{\text{melt}}, \tag{13}$$

$$\frac{d[\text{PPi}]_{\text{tot}}}{dt} = N_{\text{all}} V_{\text{tr}} - V_{\text{precip}} - V_{\text{hydrolysis}} \tag{14}$$

$$\frac{d[\text{Pi}]_{\text{tot}}}{dt} = 2 \cdot V_{\text{hydrolysis}} \tag{15}$$

$$\frac{d[\text{ATP}]_{\text{tot}}}{dt} = -N_a V_{\text{tr}} \tag{16}$$

$$\frac{d[\text{GTP}]_{\text{tot}}}{dt} = -N_g V_{\text{tr}} \tag{17}$$

$$\frac{d[\text{CTP}]_{\text{tot}}}{dt} = -N_c V_{\text{tr}} \tag{18}$$

$$\frac{d[\text{UTP}]_{\text{tot}}}{dt} = -N_u V_{\text{tr}} \tag{19}$$

$$\frac{d[H]_{\text{tot}}}{dt} = N_{\text{all}} V_{\text{tr}} \tag{20}$$

$$\frac{d[\text{T7RNAP}]_{\text{tot}}}{dt} = -k_d [\text{T7RNAP}]_{\text{tot}} \tag{21}$$

$$\frac{d[\text{Mg}]_{\text{tot}}^{(solid)}}{dt} = 2 \cdot V_{\text{precip}} \tag{22}$$

$$\frac{d[\text{Mg}]_{\text{tot}}^{(sol)}}{dt} = -2 \cdot V_{\text{precip}} \tag{23}$$

$$\frac{d[\text{dsRNA}]}{dt} = V_{\text{ann}} - V_{\text{melt}}. \tag{24}$$

2.2. Model implementation

In this study, the systems of differential-algebraic equations (DAEs) were solved using the IDA solver from the SUNDIALS suite, interfaced through the Assimulo package in Python [18].

Initial conditions for the differential equations were set based on the initial experimental concentrations of the involved species. The initial derivatives were derived from the experimentally known starting values and provided to the solver.

Consistent initial conditions for the algebraic species were computed from experimental concentration inputs using IDA's consistent-initialization routine, which adjusts the algebraic variables so that the equilibrium constraints are satisfied at t_0.

CSP and eGFP transcripts were used as model systems. These two constructs were deliberately chosen to span a wide range of the two primary sequence-level features that the model captures: transcript length (CSP: 4283 nt vs. eGFP: 995 nt) and promoter-proximal GC content (CSP: 49% vs. eGFP: 34%). The model accounts for length through per-base NTP stoichiometry (N_a, N_g, N_c, N_u) and total nucleotide count (N_{all}), and for composition through the fitted inhibition parameters k_1 and k_2. Their known sequences and corresponding nucleotide compositions are listed in SI Table D6. These template characteristics also inform the structural considerations relevant to dsRNA formation and its subsequent impact on RNA-based product quality.

Individual NTP consumption was monitored every 10 minutes across a 2 h IVT reaction. The IVT reaction was prepared as described by Welbourne et al., and the reaction was quenched at the relevant time point with 100 mM EDTA. Individual NTPs were quantified using an Anion-Exchange HPLC method [19].

2.3. Parameter estimation & experimental data

Model calibration was conducted with experimental data from 60 CSP and 30 eGFP samples, each with a replicate, using Latin Hypercube Sampling (LHS) to vary total NTP, T7RNAP, template DNA, Mg^{2+}, spermidine concentrations, and reaction time across a 6-dimensional space, ensuring equidistant sampling for comprehensive coverage (see Table D4 for parameter bounds). Independent validation was performed on a separate precipitation dataset (Section 3.1, Fig. 4) in which Mg^{2+} and PPase were varied while the kinetic parameters were held fixed at their LHS-calibrated values. Unless stated otherwise, IVT reagents (NTPs, T7RNAP, inorganic pyrophosphatase, RNase inhibitor, dithiothreitol, NaCl, Triton X-100, spermidine, and EDTA) were sourced from Roche Diagnostics GmbH, and template DNA was supplied by GenScript Biotech Corporation.

In vitro transcription (IVT) experiments were designed using *Latin Hypercube Sampling* (LHS), a space-filling method that stratifies each factor range into equally probable intervals and then combines these intervals at random. LHS ensures uniform coverage of a multidimensional input space with far fewer runs than a full factorial design while still capturing higher-order interactions among factors.

Six IVT process parameters were varied simultaneously: total NTP concentration (5–60 mM; equimolar ATP, CTP, GTP and UTP), magnesium concentration (5–90 mM; magnesium acetate), T7 RNA polymerase loading (100–400 $\text{U} \cdot \mu\text{L}^{-1}$), template DNA concentration (20–100 nM), spermidine concentration (1–4 mM), and reaction time (15–240 min). All other components were held constant: HEPES buffer (40 mM; pH adjusted with NaOH; Gibco™ 15630080), inorganic pyrophosphatase (0.05 $\text{U} \cdot \mu\text{L}^{-1}$), RNase inhibitor (1 $\text{U} \cdot \mu\text{L}^{-1}$), dithiothreitol (10 mM), sodium chloride (50 mM), Triton X-100 (0.01% v/v), and reaction temperature (37 °C). IVT reactions followed the protocol framework described by Welbourne *et al.* (2024).

After incubation, reactions were quenched with EDTA and RNA was purified by solid-phase extraction on silica spin columns using the Monarch® RNA Cleanup Kit (New England Biolabs, NEB), diluting each sample 1:2.5 in RNase-free water before following manufacturer instructions. Eluted RNA was quantified on a NanoDrop™ 2000c (Thermo Fisher Scientific) at 260 nm, with A_{260}/A_{280} and A_{260}/A_{230} ratios checked for purity.

In addition, individual NTP concentrations were quantified using the chromatographic method of Welbourne *et al.* (2024) configured for NTP measurement, providing species-resolved concentrations used for model calibration of NTP consumption dynamics (cf. Section 2.1). In this work, the Welbourne *et al.* method was used for NTP quantification, while RNA yield across the full LHS dataset was quantified using the standardized silica cleanup + NanoDrop workflow described above.

Furthermore, magnesium's role in precipitation was examined via dedicated experiments with six replicates for CSP and eGFP, varying inorganic pyrophosphatase (PPase) while maintaining constant baseline conditions: total NTP (40 mM), T7RNAP (330 $\text{U} \cdot \mu\text{L}^{-1}$), template DNA (50 nM), spermidine (3 mM), and incubation time (120 min), with Mg^{2+} (magnesium acetate) ranging from 8 to 80 mM (detailed in Table D5). Parameter estimation used a multi-start fitting approach with randomized initial guesses to approximate global minima, using the Differential Evolution (DE) optimization technique as implemented in the `scipy.optimize.differential_evolution` function in Python [20]. The NTP quantities represent the total (combined) concentration, comprising equimolar contributions of adenine (A), guanine (G), cytosine (C), and uracil (U) nucleotides.

2.4. Sensitivity analysis

A sensitivity analysis was conducted using the SALib library in Python, using Sobol sequences for 2^{20} simulations, with the objective of evaluating the model's outcome distribution in response to variations in fitted kinetic parameters, incorporating a 20% standard deviation in the fitted kinetic parameters to assess uncertainty propagation [21].

Separately, sensitivity of input concentrations was also conducted, aimed to elucidate the IVT process dependencies, whilst maintaining constant kinetic parameters with the exception of those specifically fit-

ted for CSP and eGFP transcripts, thereby discerning dependency variations across templates.

The ranges used in this sensitivity are shown in SI Tables D1 and D2.

2.5. Cost optimization

The optimization problem is formulated to minimize the total cost per unit of RNA produced, Z, which aggregates the individual costs associated with each model input and output and divides this sum by the RNA yield (see Eq. (25)). Here, "model inputs" $\{x_i\}$ are the controllable CPPs–such as NTP feed rates, enzyme loading, Mg^{2+} concentration, and reaction time–each incurring a cost coefficient C_i. "Model outputs" $\{y_j\}$ are the predicted performance metrics–such as RNA yield, individual NTP consumption, and dsRNA. This formulation applies to every species x_i (for $i = 1, \ldots, n$).

$$\text{minimize} \quad Z = \frac{\sum_{i=1}^{n} C_i x_i}{x_{RNA}(t_{\text{final}})} \tag{25}$$

To ensure the feasibility of solutions within the operational context and adhere to the parameter space, bounds for input parameters are specified (Eq. (26)).

$$\text{subject to} \quad x_{i,\min} \le x_i \le x_{i,\max}, \quad \forall i \in \{1, 2, \ldots, n\} \tag{26}$$

$$x_{RNA}(t_{\text{final}}) \ge [RNA]_{min} \tag{27}$$

$$\frac{d[\text{Mg}]_{\text{tot}}}{dt} = 0, \quad \forall t \in T \tag{28}$$

$$\frac{x_{\text{dsRNA}}(t_{\text{final}})}{x_{RNA}(t_{\text{final}})} \le 0.01, \tag{29}$$

Further constraints include maintaining a minimum RNA concentration at the process's final time step, as outlined in Eq. (27), to enforce a minimum production target under a cost-minimization objective (i.e., without any revenue/selling-price term). Additionally, Eq. (28) mandates constant total magnesium levels throughout the process, reflecting the operational necessity to minimize PPase use while preventing precipitation, thereby aligning with quality requirements.

Derived dsRNA equations (Appendix C) are applied here, with each parameter determined based on already existing experimental knowledge. This approach guarantees that the optimized solutions are practical and account for saturation effects, preventing the solution converging to unrealistically high input concentrations that do not reflect real-world conditions, and typically lead to dsRNA formation.

Cost estimates from Kis et al.'s study assume a manufacturing scale large enough to benefit from economies of scale, effectively minimizing per-unit costs [22]. This scale implies not only a high production capacity but also optimized resource utilization and supply chain efficiencies, negating the need for additional scaling costs considerations.

The problem was solved using the Broyden-Fletcher-Goldfarb-Shanno (BFGS) algorithm, as implemented in the `scipy.optimize` module in Python [20].

3. Results & discussion

A quantitative bioprocess model was developed, employing bi-substrate kinetic equations adapted from previous multiphysics models to calculate RNA transcription yield. The key CPPs included in the model are initial NTP concentration, Mg^{2+} concentration, T7RNAP concentration, template DNA concentration, spermidine concentration, and reaction time. This includes the formation of all relevant complexes. Additionally, the type of template DNA, sequence length, and NTP composition of the specific template DNA were considered as CMAs. The model also tracks NTP consumption over time and final concentrations, providing insights into process efficiency. The remaining CPPs were controlled using standard bioreactor setups compliant with cGMP guidelines.

Table 1
Fitted kinetic parameters for both CSP and eGFP template DNA, with model performance metrics. LHS rows report calibration-set fit quality; precipitation rows report independent validation-set performance. Metrics include R^2, Relative Root Mean Square Error (RRMSE), and Relative Mean Percent Square Error (RMPSE).

Parameter / Metric	Unit	CSP	eGFP
k_{app}	$mM^{-1}s^{-1}$	0.00125	0.00125
k_1	mM^{-1}	2	17
k_2	mM^{-1}	31	0.2
k_{precip}	s^{-1}	5	5
k_{PPase}	mM	3120	3120
R^2 (LHS)	-	0.851	0.868
R^2 (Precipitation)	-	0.886	0.921
$RRMSE$ (LHS)	%	28.4	26.7
$RRMSE$ (Precipitation)	%	15.4	11.5

This approach links process understanding to QbD-driven design-space definition.

An initial fit of the kinetic parameters was performed utilizing the entirety of the dataset (cf. Section 2.3 Parameter Estimation). Preliminary assumptions were made to streamline the fitting process; notably, the absence of mRNA degradation observed in the experimental data led to the exclusion of k_{ac}, k_{ba}, and k_{Mg} from the fitting process by setting these parameters to zero. Due to the lack of reliable methods to measure and quantify dsRNA, parameters and equations related to dsRNA have also been excluded here.

The equilibrium parameter K_{12} was determined through fitting, due to its initially undetermined value in the experimental setup. This process ensured the parameter's consistency across various kinetic and experimental conditions, yielding a stable value of $K_{12} = 110mM^{-2}$ for both templates. The identical values, representing the interaction between T7RNAP, template DNA and spermidine, highlight the enzyme's binding affinity to the DNA, which is primarily influenced by specific promoter sequences rather than the overall sequence length and composition between the templates. This suggests that the promoter sequences provide a consistent chemical and physical framework for T7RNAP interaction across varying DNA templates.

A practical consideration for deployment is that the fitted kinetic parameters reflect the activity of the specific T7RNAP preparation under the stated buffer and temperature conditions. While the model structure is not tied to a particular T7RNAP manufacturer, switching supplier or lot may require re-identification of a small subset of effective activity parameters (at minimum k_{app}, and where relevant, throughput/initiation terms), while retaining the same governing equations. Since T7RNAP showed no measurable loss of activity over the 0.25–4 h reactions, we fixed the deactivation rate to $k_d = 0\,\text{min}^{-1}$ as a modeling assumption to avoid overfitting. Subsequent calibration therefore targeted k_{app}, k_1, k_2, k_{precip}, k_{PPase}.

3.1. Model calibration and validation against LHS experimental data

Kinetic parameters were independently fitted for the production of mRNA encoding the SARS-CoV-2 Spike protein (CSP) and enhanced green fluorescent protein (eGFP) templates in an IVT reaction. For the CSP and eGFP transcripts, 60 and 30 experimental data points were generated via Latin hypercube sampling (LHS), respectively. Given the utilization of excess inorganic pyrophosphatase (PPase) in the LHS experiments, precipitation was assumed negligible and the precipitation flux was disabled for those conditions (i.e., we set $V_{\text{precip}} = 0$ during LHS calibration). The precipitation coefficient k_{precip} was subsequently identified using the dedicated precipitation dataset described in Section 3.2; Table 1 reports the combined parameter set used for subsequent simulations.

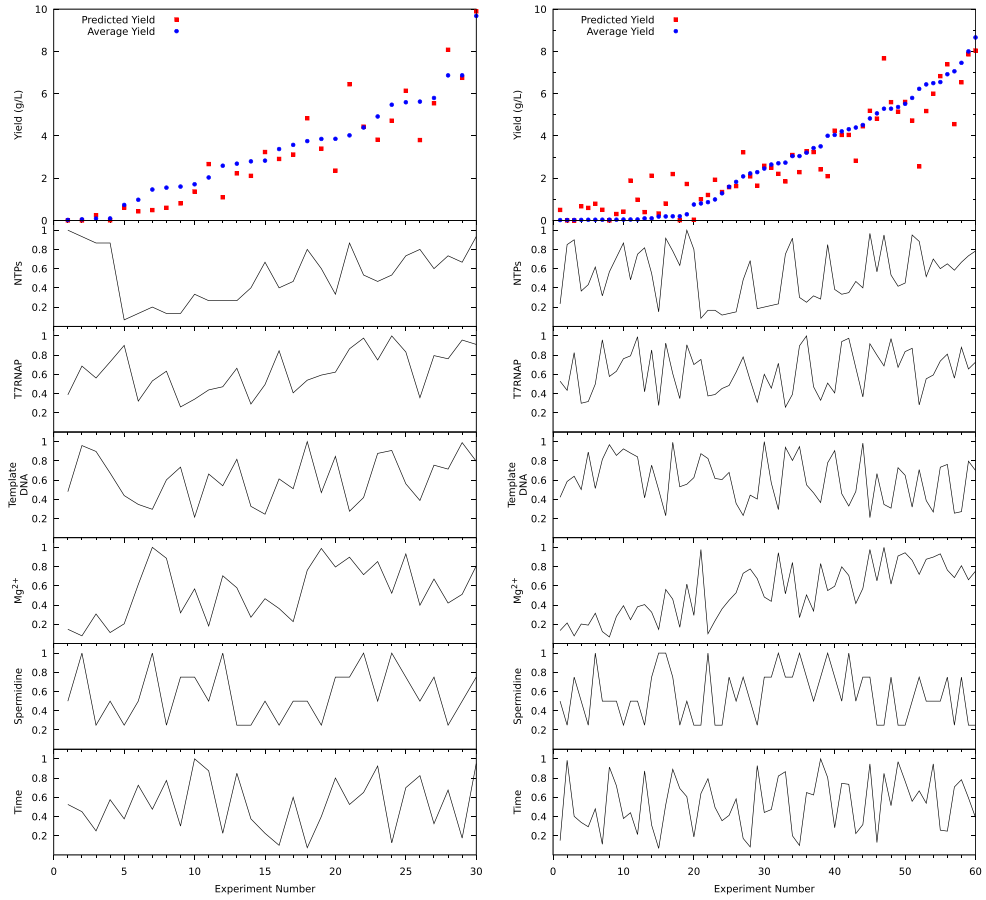

Fig. 2. Experimental and model predicted mRNA yield for eGFP and CSP. (a) 30 experimental Latin hypercube sampling (LHS) data points for eGFP; (b) 60 experimental LHS data points for CSP. Blue points denote the mean of two experimental replicates; red squares are model predictions. Within each panel, points are ordered by increasing experimental yield. Experimental conditions listed beneath the panels include concentrations of NTP, T7RNAP, DNA template concentration, Mg^{2+}, spermidine, and the reaction time. Scatter in the experimental values reflects the LHS design used to vary these critical process parameters. Note that reaction time is treated as a sixth experimental variable in the LHS design: each condition is sampled at a single endpoint rather than as a time-course, so that the full 6-dimensional input space is covered with minimal experimental effort. (For interpretation of the references to colour in this figure legend, the reader is referred to the web version of this article.)

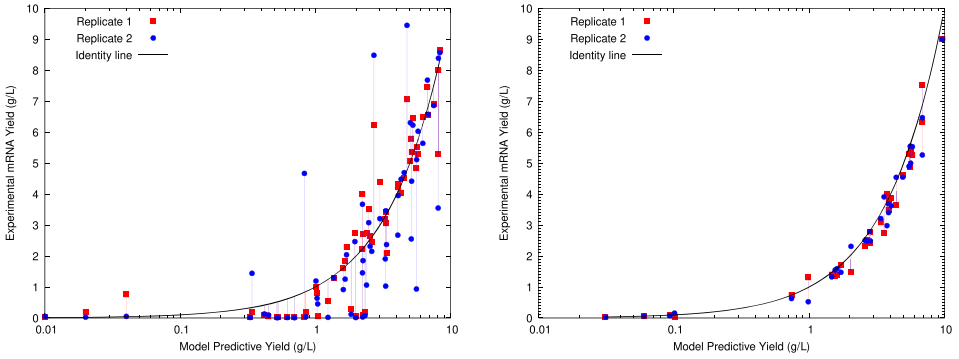

(a) Parity plot for CSP mRNA from LHS experiments.

(b) Parity plot for eGFP mRNA from LHS experiments.

Fig. 3. Parity plots comparing model predictions with experimental *mRNA* yields for (a) CSP and (b) eGFP. Both axes are on a $\log_{10}$ scale, and the black line is the identity line $y = x$. Each point represents a single replicate under a given condition (red squares: replicate 1; blue circles: replicate 2). Line segments connect the two replicates run under the same condition to visualize replicate dispersion. (For interpretation of the references to colour in this figure legend, the reader is referred to the web version of this article.)

Fig. 2 illustrates the correlation between model predictions and experimental RNA yields obtained through Latin Hypercube Sampling (LHS) for CSP and eGFP template DNAs, including the corresponding experimental conditions. Fig. 3 shows the relationship between the true experimental RNA yields (x-axis) and the model's predictions (y-axis), with closer alignment to the identity line indicating more accurate predictions. A logarithmic scale is used here as the data spans several orders of magnitude, including many smaller yield values.

Replicate scatter is present across the full yield range and is attributable to *measurement noise* in the silica-column purification and A_{260}-based (NanoDrop) quantification workflow. At the low end of the spectrum (below ~1 g L^{-1}), column recovery losses can approach the total sample mass, so that one replicate may return a near-zero reading while the other retains measurable material; these discrepancies, while visually prominent on the parity plot, are small in absolute terms (g L^{-1}). At high yields, the same sources of variability—differences in effective enzyme activity, template quality, mixing/pipetting, and downstream recovery—translate into larger absolute deviations that dominate the RRMSE. This effect is more apparent under an LHS design because the operating domain is intentionally broad, increasing the likelihood of sampling steep regions of the response surface where measurement variability has a larger impact on the observed output. Replicate dispersion is higher for CSP than for eGFP, consistent with the longer transcript being more sensitive to run-to-run differences in RNAP activity and template integrity, as well as length-dependent recovery losses in the purification workflow.

Despite this scatter, the model achieves R^2 values of 0.851 and 0.868 for CSP and eGFP respectively on the LHS dataset. Prior mechanistic IVT models are typically parameterized on narrower, factorial DoE designs, and empirical regression approaches can generalize poorly to new operating points. The model's ability to capture yield trends across a broad, 6-dimensional operating space and two templates of contrasting length and composition therefore represents a meaningful advance; targeted replication near the upper-yield boundary would be the most direct route to further tighten predictive accuracy.

While k_{app} remained consistent across both sequences, the individual rate constants, k_1 and k_2, showed significant differences. Specifically, k_1, which is associated with Mg^{2+} inhibition, and k_2, linked to the inhibition by the Mg-NTP complex, displayed contrasting behaviors between the CSP and eGFP sequences. In the case of the CSP sequences, Mg^{2+} inhibition was reduced, whereas inhibition by the Mg-NTP complex increased.

This difference may be associated with sequence composition in the promoter-proximal transcribed region downstream of the T7 promoter (Table D6), which is more GC-rich for CSP than for eGFP (49.06% vs 34.04% respectively). GC rich sequences are well documented to enhance DNA structural integrity due to stronger hydrogen bonding and improved base stacking interactions [23]. These properties can increase the stability of RNA–DNA hybrids and transcription bubbles, influencing transcriptional dynamics. While high GC content may reduce flexibility in these structures, it could also diminish the inhibitory effects of free Mg^{2+} ions by stabilizing nucleic acid conformations [24]. However, this added stability may impose kinetic constraints on the transcription complex, requiring RNA polymerase to exert additional energy to unwind the DNA and elongate the RNA strand [25].

Related sequence features could contribute alongside GC content. Promoter proximal folding free energy (ΔG) and the presence of pause or abort motifs can affect initiation and promoter escape, and early3′ design and local composition in the first tens of nucleotides can modulate early elongation behaviour [26,27]. These effects may contribute to the observed CSP–eGFP differences alongside GC content.

Under typical conditions, free Mg^{2+} is essential for transcription, acting as a cofactor to stabilize NTPs and facilitate their incorporation into the nascent RNA strand [28]. At the same time, excess free Mg^{2+} can nonspecifically bind to nucleic acids, potentially inhibiting transcription, particularly in regions where flexibility in the transcription bubble is necessary [24]. For templates with a more GC-rich promoter-proximal region, the increased stability of the RNA–DNA hybrid may mitigate these inhibitory effects, shifting the transcription complex's dependency toward Mg-NTP complexes for energy and stability during elongation [26].

Taken together, this mechanistic picture suggests how sequence may map onto our kinetic terms without changing the current model: factors that influence initiation and promoter escape (e.g., GC fraction, promoter proximal ΔG, pause/abort motifs) would primarily manifest in an apparent k_1, whereas features that influence early elongation (e.g., early3′ design and local structure) would be reflected in an apparent k_2. In the present study, k_1 and k_2 were treated as sequence agnostic; thus, the CSP–eGFP interpretation above is explanatory rather than causal and should be treated as a hypothesis given that only two templates are analysed here. As future work, one could explicitly test this hypothesis by re-parameterizing k_1 and k_2 as functions of such sequence descriptors and evaluating whether this improves fit and predictive power [23–28].

3.2. Model performance in capturing precipitation dynamics

Once the kinetic parameters were established, they were used as initial guesses to fit the precipitation parameters, against 18 datapoints where the amount of Mg^{2+} and PPase is varied. We aimed to determine whether the same kinetic parameters could also accurately describe the precipitation kinetics, alongside the newly fitted precipitation parameters. This approach validates the robustness of the initially determined kinetic parameters and ensures that the precipitation parameters are accurately characterized without overfitting.

The precipitation-specific data points yielded higher R^2 values for both templates (0.886 and 0.921 for CSP and eGFP respectively shown in Fig. 4) compared to the LHS design predictions. This improvement is, however, attributed to the smaller and simplified variable set in the precipitation experiments.

The kinetic parameters for precipitation were fitted independently to each template dataset using identical initial guesses, with both optimizations converging to identical values, indicating consistent precipitation kinetics across templates. This observation aligns with the theoretical expectation that the rate of precipitation is independent of the template used, being primarily captured by the kinetics of RNA synthesis only. The ability of these original kinetic parameters to accurately describe both the LHS and the precipitation-specific data confirms that they are reliable across different experimental conditions.

In precipitation scenarios, the model appears to capture the potential consequences of reduced Mg^{2+} availability. Mechanistically, this aligns with expectations: altering PPase concentrations shifts the optimal Mg^{2+} level required for maximizing yield. For the eGFP template, increasing both Mg^{2+} and PPase beyond a certain threshold reduces yield, suggesting that Mg^{2+} may act as an inhibitor under these conditions [15]. In contrast, at lower PPase concentrations, this inhibitory effect is less apparent, as Mg^{2+} is consumed to form precipitate. The CSP template, by comparison, exhibits different behavior. Rather than showing clear inhibition, it may fail to achieve an optimal yield due to insufficient Mg^{2+} levels. These observations support the interpretations presented in Section 3.1, where it was proposed that eGFP could be more susceptible to Mg^{2+} inhibition than CSP, potentially due to differences in GC content.

The precipitation results therefore support the validity of the kinetic parameters identified from the LHS dataset.

3.3. NTP consumption analysis

Fig. 5 presents a comparative analysis between the modeled and experimental data on NTP consumption over time from AEX-HPLC for the eGFP construct under a single experimental composition. The time-course was generated by running replicate reactions at the same condition and quenching at predefined time points (i.e., discrete time-point experiments), rather than continuous sampling from one reactor. The

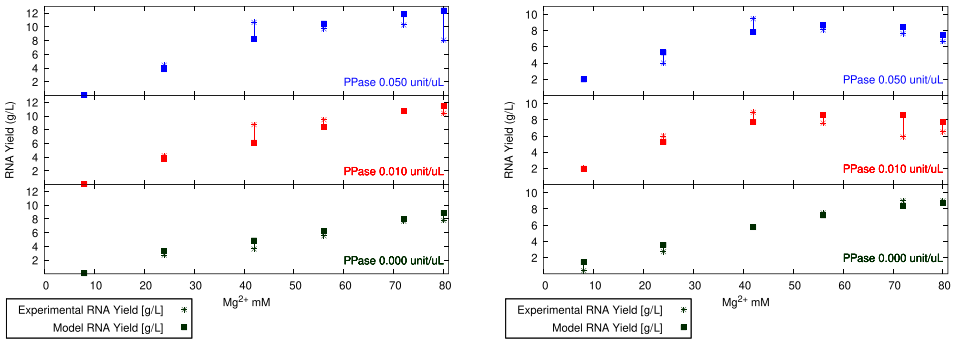

(a) CSP sequences results. (b) eGFP sequences results.

Fig. 4. RNA yield as a function of Mg^{2+} concentration and PPase levels for CSP and eGFP transcripts. The figures compare experimental and model-predicted RNA yields under varying Mg^{2+} concentrations (10-80 mM) and PPase levels: 0 $unit \cdot \mu L^{-1}$ (green), 0.010 $unit \cdot \mu L^{-1}$ (red), and 0.050 $unit \cdot \mu L^{-1}$ (blue). Experimental RNA yield (star markers) and model-predicted RNA yield (square markers) are plotted for each condition. Other Reaction conditions were fixed at 40 mM total NTPs, 330 $unit \cdot \mu L^{-1}$ T7 RNA polymerase, 2 mM spermidine, 50 nM DNA, and a 2-hour reaction time. (For interpretation of the references to colour in this figure legend, the reader is referred to the web version of this article.)

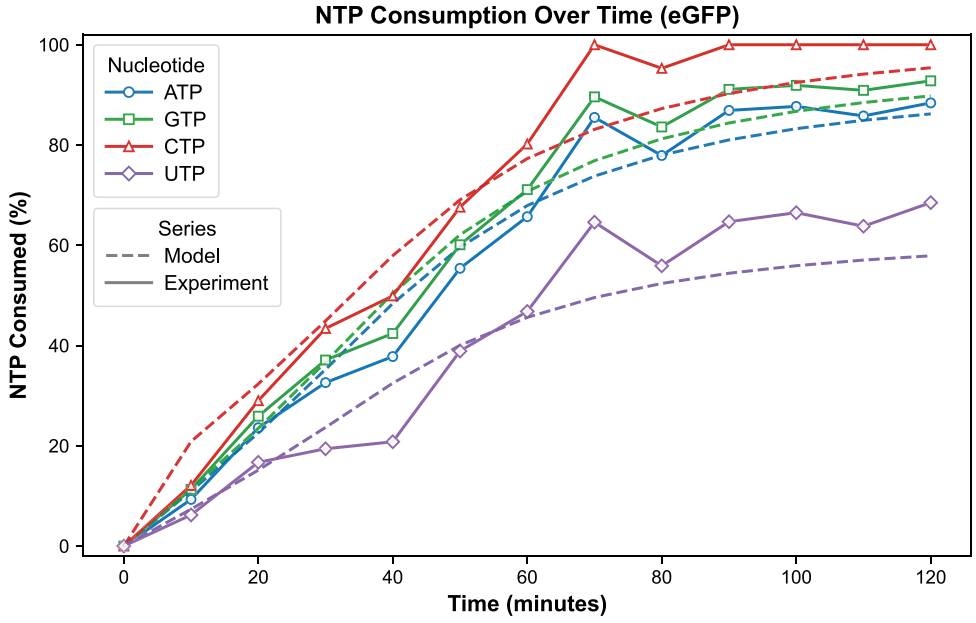

Fig. 5. Comparison of experimental and model predicted NTP concentrations over 0-120 min, measured by anion-exchange HPLC (AEX-HPLC). Experimental measurements are shown as markers (continuous lines): ATP (blue circles), GTP (green squares), CTP (red triangles), and UTP (purple diamonds). Model predictions are shown as *continuous dotted lines* in the same colors. Time-course points were obtained from replicate reactions quenched at predefined time points under a single experimental composition (eGFP). (For interpretation of the references to colour in this figure legend, the reader is referred to the web version of this article.)

model captures the overall trend in NTP consumption with reasonable accuracy. However, minor deviations are observed in the final consumption values. Experimental discrepancies noted at 80 and 110 minutes, where non-monotonic changes in measured NTP levels are recorded, and are attributed to experimental variability across discrete time-point runs. Such variations highlight the challenges in experimental consistency.

Importantly, the relative depletion of each NTP is consistent with the template-specific nucleotide composition reported in Table D6: starting from equimolar NTP concentrations, nucleotides with lower sequence demand (notably UTP for eGFP) remain in relative excess, whereas the limiting nucleotide is depleted first and ultimately caps further transcription. mRNA was not quantified as a time-course in this AEX-HPLC experiment (RNA yield is measured separately at the final time point as reported in Fig. 3). An accurate RNA prediction would also imply accuracy in NTP consumption modeling. Any remaining inaccuracies could reflect unaccounted sinks for NTP, such as stable complexes or unintended side reactions consuming NTP. The model captures most of these effects nonetheless (cf. Section 2.1 Model Formulation).

3.4. Sensitivity insights: key drivers of model response

Global sensitivity analysis (GSA) was performed, and the first, and second-order Sobol indices were computed to evaluate the impact of various parameters on RNA yield.

Fig. 6(a) and (b) present Sobol sensitivity indices for the kinetic parameters, quantifying their influence on RNA yield variability for CSP and eGFP transcripts. For both templates, k_{app} was the most influential parameter, contributing the majority of the variance in RNA yield, highlighting its critical role in determining transcription efficiency.

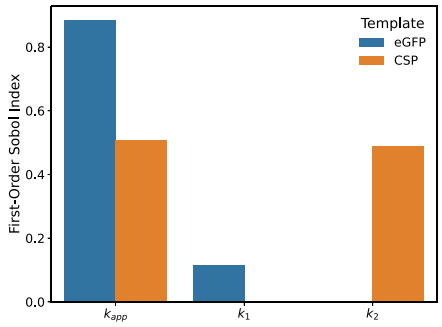

(a) Kinetic: First-order indices

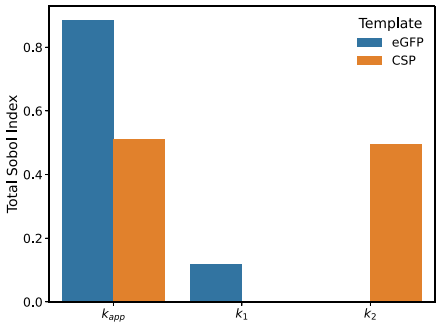

(b) Kinetic: Total-order indices

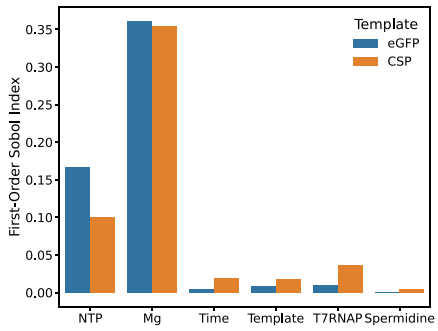

(c) CSP/eGFP: First-order indices

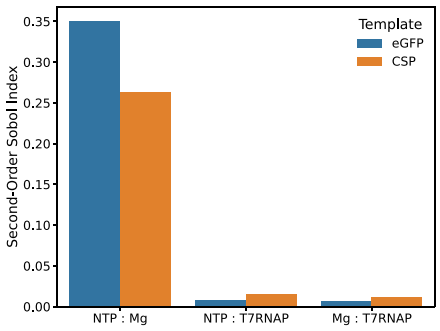

(d) CSP/eGFP: Second-order indices

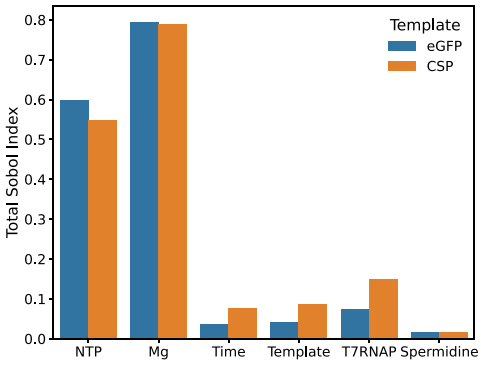

(e) CSP/eGFP: Total-order indices

Fig. 6. Sobol Sensitivity Analyses. Sobol indices explore how variations in model parameters affect RNA yield across both CSP and eGFP transcripts. Subfigures (a) and (b) depict first-order and total-order Sobol indices when the *fitted kinetic parameters* are varied by ±20% (standard deviation). Subfigures (c), (d), and (e) then examine the sensitivity of *input concentrations* while holding the kinetic parameters constant (except for those specifically fitted to each template).

For CSP, k_1 had minimal impact, while k_2 was almost as significant as k_{app}, reflecting CSP's reliance on Mg-NTP complexes to overcome the rigidity of its GC-rich transcription bubble. In contrast, for eGFP, k_{app} dominated, accounting for 88% of the variance, with k_1 contributing 12%. k_2 was negligible for eGFP, consistent with its reduced reliance on Mg-NTP complexes to sustain transcription.

The identical first-order and total-order indices for both templates suggest that RNA yield variability may arise primarily from the independent contributions of k_{app}, k_1, and k_2, with no substantial interaction effects. However, the mechanistic roles of these parameters may differ between templates: CSP's high GC content potentially reduces Mg^{2+}-mediated inhibition and shifts dependency toward Mg-NTP complexes, while eGFP's lower GC content could lead to greater sensitivity to free Mg^{2+} inhibition and influence overall elongation efficiency.

Fig. 6(c)–(e) present the first-order, second-order, and total-order Sobol sensitivity indices for the input parameters influencing CSP and eGFP transcripts.

eGFP exhibited stronger first-order sensitivity to NTP and, to a lesser extent, Mg^{2+}, compared to CSP. This could reflect eGFP's reliance on nucleotide availability for maintaining elongation efficiency and its increased susceptibility to free Mg^{2+} inhibition. CSP, by contrast, showed lower sensitivity to individual parameters, possibly due to greater intrinsic stability of the transcription bubble, which may reduce dependency on external factors. Across both templates, spermidine exhibited comparatively low first-order and total-order sensitivity within the explored 1–4 mM range, indicating it is not a primary driver of yield variability under these conditions.

Second-order indices suggest eGFP's greater reliance on Mg-NTP interactions, highlighting the potential importance of coordinated

magnesium dynamics and nucleotide incorporation. While CSP may depend on Mg-NTP complexes to overcome transcription bubble rigidity, its stable bubble could minimize sensitivity to perturbations in these interactions. By contrast, eGFP's more flexible transcription bubble might amplify its sensitivity to such variability.

Total-order indices further indicate that eGFP could be more sensitive overall to NTP and Mg^{2+} compared to CSP. Together, these findings are consistent with sequence-dependent transcriptional dynamics: CSP's higher GC content may shift reliance toward stable Mg-NTP interactions, whereas eGFP's lower GC content could increase its sensitivity to both free Mg^{2+} and Mg-NTP coordination.

3.5. Model-based cost optimization

By exploring the model's parameter space, we identified an optimal set of reaction conditions to minimize the overall cost per gram of RNA produced (not including capping costs as these are assumed to be fixed). Under these conditions—39 mM total NTP, 297 U mL^{-1} T7RNAP, 54 mM Mg^{2+}, 101 nM DNA, and 0.38 mM PPase over a 121-minute reaction—the model predicts a yield of 7.28 g L^{-1}, corresponding to $6,772 per gram of RNA on a 1 L basis (individual unit prices and conversions are reported in SI Table D3). In this work, IVT conditions primarily influence $/g through their impact on IVT reagent consumption and the grams of RNA produced per batch volume. We also note that absolute $/g values are sensitive to procurement assumptions (e.g., list versus contract pricing, grade, and supplier), and therefore the reported cost should be interpreted as an illustrative baseline used to compare operating points consistently within the model, rather than a universal manufacturing quote.

The model naturally favors conditions that reduce the most expensive inputs (notably NTPs), since lower NTP charges can reduce direct reagent spend while maintaining sufficient yields and quality. At the same time, the optimum is not achieved simply by increasing initial NTP concentration, because RNA yield and NTP utilization depend on the coupled NTP–Mg^{2+} balance and the identity of the limiting nucleotide. We do not assume complete conversion of all four NTP species to product RNA: transcription is limited by the first-depleted nucleotide, so any non-limiting nucleotide (e.g., UTP for eGFP under equimolar starting conditions; cf. Fig. 5) may remain partially unconsumed. This residual is still costed in the objective because reagent spend is based on the initial concentrations, and therefore higher initial NTP can increase RNA mass but does not necessarily improve conversion or reduce $/g if a larger overage remains unused. Allowing non-equimolar initial NTP ratios matched to template composition (particularly important for expensive modified NTPs) is a natural extension that could reduce residual overage while maintaining yield.

Also note that recycling is not considered here, which would drastically reduce material costs. Related process-intensification strategies such as fed-batch IVT have also been proposed to improve NTP utilization and reduce cost [29–31].

4. Conclusion

The COVID-19 pandemic highlighted the need for rapid, scalable mRNA manufacturing. In this work we introduced a mechanistic bioprocess model constructed entirely from first principles—thermodynamic equilibria, enzyme kinetics, and stoichiometric mass balances—that integrates QbD principles into the optimization of mRNA therapeutics manufacturing. Experimental data serve only a support role: a small set of effective kinetic parameters is calibrated, while all remaining model structure is derived from established physicochemical knowledge. By systematically mapping relationships between CPPs, CMAs, and RNA yield, the model provides a practical tool for IVT process design that is applicable across templates and operating conditions.

A central hypothesis explored in this study was the role of template-specific sequence composition in transcriptional dynamics, particularly through dependencies on Mg^{2+} and Mg-NTP interactions. GSA identified distinct sensitivities, with the kinetic parameter k_2 (associated with Mg-NTP-mediated inhibition) exerting a stronger influence on IVT producing CSP than eGFP. These differences reflect underlying sequence-dependent physicochemical factors, such as GC content, transcription bubble stability, and the interplay between enzyme activity and substrate availability. These findings highlight the need for a tailored approach to reaction conditions, where template composition informs process design for encoding diverse vaccine antigens, therapeutic proteins, or gene-editing components.

Beyond the empirical sensitivity contrast, it is important to note that our current formulation deliberately *lumps* template-dependent biophysical effects into two effective kinetic knobs: k_1 and k_2. This lumping makes the model compact and transferable across transcripts, but it also provides a natural bridge for future mechanistic unpacking. In particular, k_1 and k_2 can be re-parameterized as functions of sequence-level descriptors (e.g., GC%, predicted folding ΔG in promoter-proximal windows, pause/abort motifs, and3′ design). Thus, while the present study treats k_1 and k_2 as template-specific surrogates, they were chosen so that subsequent work can map them to biochemically interpretable quantities without altering the overall model structure.

More broadly, mechanistic models of the kind presented here can reduce the number of experiments needed to establish a viable operating window, lowering both development time and reagent costs. This is particularly relevant for emerging mRNA programs where rapid template switching is required and large-scale DoE campaigns are impractical.

A key limitation is interpretability of the lumped parameters: template sequence, nascent RNA structure, and Mg-driven speciation all project onto k_1 and k_2. This was an explicit design choice to keep the optimization tractable and data-efficient. Nevertheless, the same structure enables hierarchical extensions in which k_1 and k_2 are endowed with sequence-informed priors, or are decomposed into initiation- and elongation-specific sub-parameters constrained by literature stability constants for Mg complexes. Such extensions would preserve tractability while increasing biochemical fidelity and transferability to novel templates.

Future work should also extend this model by incorporating additional reaction complexities, including alternative capping strategies, modified nucleotides, and novel polymerase variants with altered substrate or temperature dependencies. The dsRNA sub-model presented in Appendix C has not yet been experimentally validated; established quantification methods (e.g., J2 antibody ELISA, dot blot, or dedicated AEX-HPLC) exist and should be employed in future studies to validate the dsRNA predictions and incorporate dsRNA as a fully validated CQA alongside yield. Similarly, applying established mRNA integrity assays (e.g., capillary electrophoresis) and characterizing intermediate complexes will further strengthen the model. Integration of real-time feedback for dynamic process adjustments could also facilitate closed-loop manufacturing systems, enabling next-generation bioprocessing.

As regulatory expectations for advanced therapeutics evolve, the QbD-driven approach outlined here ensures robust, reproducible, and transparent manufacturing protocols that meet stringent quality standards and expedite regulatory approval.

In conclusion, this study advances IVT process development by connecting mechanistic insights to QbD-driven optimization. The framework provides researchers and manufacturers with a mechanistically grounded tool to support process design for mRNA therapeutics. Extension to additional constructs, experimentally validated dsRNA and integrity CQAs, and scale-dependent considerations will be necessary to realize the full potential of this approach in manufacturing settings.

Funding

This study was funded by Wellcome Leap R3 Program. The funder played no role in study design, data collection, analysis and interpretation of data, or the writing of this manuscript.

Ethics approval

Not applicable

Consent to participate

Not applicable

Consent for publication

Not applicable

Availability of data and materials

Not applicable

Code availability

Not applicable

Data availability

Data will be made available on request.

CRediT authorship contribution statement

Mahdi Ahmed: Writing – review & editing, Writing – original draft, Visualization, Validation, Software, Methodology, Investigation, Formal analysis, Conceptualization; **Aditya Nair:** Formal analysis, Data curation; **Joseph Middleton:** Writing – review & editing, Visualization; **Kate Loveday:** Data curation; **Solomon Brown:** Writing – review & editing, Supervision, Funding acquisition, Conceptualization; **Zoltan Kis:** Writing – review & editing, Supervision, Funding acquisition, Conceptualization; **Joan Cordiner:** Writing – review & editing, Supervision, Funding acquisition, Conceptualization.

Declaration of competing interests

The authors declare the following financial interests/personal relationships which may be considered as potential competing interests: Zoltan Kis reports financial support was provided by Wellcome Leap Fund. Zoltan Kis reports a relationship with Coalition for Epidemic Preparedness Innovations that includes: funding grants. If there are other authors, they declare that they have no known competing financial interests or personal relationships that could have appeared to influence the work reported in this paper.

Acknowledgments

Thanks to Mabrouka Maamra, Emma Welbourne, Mark Dickman, Lewis Ufton, and Ioanna Kalospyrou.

Appendix A. Extended Equations

Notation. Let $\mathcal{B} = \{\mathrm{ATP}, \mathrm{CTP}, \mathrm{GTP}, \mathrm{UTP}\}$ index the four NTPs; quantities with subscript b are base-specific.

$$\begin{aligned} NTP_{\mathrm{tot}} = \sum_{i\in\mathcal{I}} \Big(& [NTP_i^{4-}] \\ & + [MgNTP_i^{2-}] \\ & + [Mg_2NTP_i^{4-}] \\ & + [MgHNTP_i^{3-}] \\ & + [HNTP_i^{3-}] \Big). \end{aligned} \tag{A.1}$$

For precipitation, we group pyrophosphate into non-Mg-bound ("free") and Mg-bound forms:

$$[PPi]_{\mathrm{free}} = [PPi^{4-}] + [HPPi^{3-}] + [H_2PPi^{2-}], \tag{A.2}$$

$$[PPi]_{\text{Mg-bound}} = [MgPPi^{2-}] + [Mg_2PPi^{4-}] + [MgHPPi^{3-}], \tag{A.3}$$

$$PPi_{\mathrm{tot}} = [PPi]_{\mathrm{free}} + [PPi]_{\text{Mg-bound}}. \tag{A.4}$$

$$\begin{aligned} H_{\mathrm{tot}} = {} & [H^+] \\ & + [HHEPES] \\ & + \sum_{i\in\mathcal{I}} \left([HNTP_i^{3-}] + [MgHNTP_i^{3-}] \right) \\ & + [HPPi^{3-}] \\ & + [MgHPPi^{3-}] \\ & + [H_2PPi^{2-}] \\ & + [HPi^{2-}] \\ & + [H_2Pi^-] \\ & + [H_3Pi] \\ & + [HAc]. \end{aligned} \tag{A.5}$$

$$\begin{aligned} T7RNAP_{\mathrm{tot}} = {} & [T7RNAP] \\ & + [\mathrm{DNA}^- \cdot T7RNAP] \\ & + [\mathrm{DNA}^- \cdot T7RNAP \cdot \mathrm{Spd}^{3+}]. \end{aligned} \tag{A.6}$$

$$\begin{aligned} \mathrm{Spd}_{\mathrm{tot}} = {} & [\mathrm{Spd}^{3+}] \\ & + [\mathrm{DNA}^- \cdot \mathrm{Spd}^{3+}] \\ & + [T7RNAP \cdot \mathrm{Spd}^{3+}] \\ & + [\mathrm{DNA}^- \cdot T7RNAP \cdot \mathrm{Spd}^{3+}]. \end{aligned} \tag{A.7}$$

$$\begin{aligned} \mathrm{DNA}_{\mathrm{tot}} = {} & [\mathrm{DNA}^-] \\ & + [\mathrm{DNA}^- \cdot T7RNAP] \\ & + [\mathrm{DNA}^- \cdot \mathrm{Spd}^{3+}] \\ & + [\mathrm{DNA}^- \cdot T7RNAP \cdot \mathrm{Spd}^{3+}]. \end{aligned} \tag{A.8}$$

$$\begin{aligned} Mg_{\mathrm{tot}}^{(\mathrm{sol})} = {} & [Mg^{2+}] \\ & + \sum_{i\in\mathcal{I}} \left([MgNTP_i^{2-}] + 2[Mg_2NTP_i^{4-}] + [MgHNTP_i^{3-}] \right) \\ & + [MgHPPi^{3-}] \\ & + [MgHPi] \\ & + [MgAc]^+ \\ & + [MgAc_2]. \end{aligned} \tag{A.9}$$

Equation (A.9) includes only *solution-phase* magnesium. Any precipitated magnesium pyrophosphate is tracked separately as a solid.

$$Mg_{\mathrm{tot}}^{(\mathrm{solid})} = [Mg_2PPi]_{(s)} + [MgPPi^{2-}]_{(s)} + [MgHPPi^{3-}]_{(s)}, \tag{A.10}$$

$$Mg_{\mathrm{tot}}^{(\mathrm{sys})} = Mg_{\mathrm{tot}}^{(\mathrm{sol})} + Mg_{\mathrm{tot}}^{(\mathrm{solid})} \tag{A.11}$$

$$\begin{aligned} HEPES_{\mathrm{tot}} = {} & [HEPES] \\ & + [HHEPES]. \end{aligned} \tag{A.12}$$

$$\begin{aligned} Pi_{\mathrm{tot}} = {} & [Pi^{3-}] \\ & + [HPi^{2-}] \\ & + [H_2Pi^-] \\ & + [H_3Pi] \\ & + [MgHPi]. \end{aligned} \tag{A.13}$$

$$Ac_{\mathrm{tot}} = [Ac^-]$$

$$+ [HAc]$$
$$+ [MgAc]^{+}$$
$$+ 2[MgAc_2]. \tag{A.14}$$

$$[Mg^{2+}][NTP_i^{4-}] = K_{1,i}\,[MgNTP_i^{2-}], \tag{A.15}$$
$$[Mg^{2+}][MgNTP_i^{2-}] = K_{2,i}\,[Mg_2NTP_i^{4-}], \tag{A.16}$$
$$[Mg^{2+}][HNTP_i^{3-}] = K_{3,i}\,[MgHNTP_i^{3-}], \tag{A.17}$$
$$[H^{+}][NTP_i^{4-}] = K_{4,i}\,[HNTP_i^{3-}], \tag{A.18}$$

(for each $i \in 1$; if base-independent, set $K_{k,i} = K_k$).

$$[H^{+}][PPi^{4-}] = K_5\,[HPPi^{3-}], \tag{A.19}$$
$$[H^{+}][HPPi^{3-}] = K_6\,[H_2PPi^{2-}], \tag{A.20}$$
$$[Mg^{2+}][HPPi^{3-}] = K_7\,[MgHPPi^{3-}], \tag{A.21}$$
$$[Mg^{2+}][PPi^{4-}] = K_8\,[MgPPi^{2-}], \tag{A.22}$$
$$[Mg^{2+}][MgPPi^{2-}] = K_9\,[Mg_2PPi^{4-}], \tag{A.23}$$
$$[H^{+}][HEPES] = K_{10}\,[HHEPES], \tag{A.24}$$
$$[\mathrm{DNA}^{-}][T7RNAP] = K_{11}\,[\mathrm{DNA}^{-}\cdot T7RNAP], \tag{A.25}$$
$$[\mathrm{DNA}^{-}][T7RNAP][\mathrm{Spd}^{3+}] = K_{12}\,[\mathrm{DNA}^{-}\cdot T7RNAP\cdot \mathrm{Spd}^{3+}], \tag{A.26}$$
$$[\mathrm{DNA}^{-}][\mathrm{Spd}^{3+}] = K_{13}\,[\mathrm{DNA}^{-}\cdot \mathrm{Spd}^{3+}], \tag{A.27}$$
$$[T7RNAP][\mathrm{Spd}^{3+}] = K_{14}\,[T7RNAP\cdot \mathrm{Spd}^{3+}], \tag{A.28}$$
$$[H^{+}][Pi^{3-}] = K_{15}\,[HPi^{2-}], \tag{A.29}$$
$$[H^{+}][HPi^{2-}] = K_{16}\,[H_2Pi^{-}], \tag{A.30}$$
$$[H^{+}][H_2Pi^{-}] = K_{17}\,[H_3Pi], \tag{A.31}$$
$$[Mg^{2+}][HPi^{2-}] = K_{18}\,[MgHPi], \tag{A.32}$$
$$[H^{+}][Ac^{-}] = K_{19}\,[HAc], \tag{A.33}$$
$$[Mg^{2+}][Ac^{-}] = K_{20}\,[MgAc]^{+}, \tag{A.34}$$
$$[MgAc]^{+}[Ac^{-}] = K_{21}\,[MgAc_2]. \tag{A.35}$$

All equilibrium parameters can be found in Table D7

Appendix B. Throughput-ceiling extended

We cap the intrinsic transcription rate V_{raw} by

$$V_{\max} = \min\{V_{\mathrm{unit}},\, V_{\mathrm{part}}\}, \qquad V_{\mathrm{tr}} = \min\{V_{\mathrm{raw}},\, V_{\max}\}.$$

By the conventional Unit definition for T7 RNAP (one Unit incorporates 1 nmol of NTP *in 60 min* at 37°C),

$$F_{\mathrm{Unit}} = \left(\frac{1\,\mathrm{nmol}}{60\,\mathrm{min}}\right)\left(\frac{10^6\,\mu\mathrm{L}}{1\,\mathrm{L}}\right) = 1.667\times10^{-5}\ \mathrm{mol\,L^{-1}\,min^{-1}\ per\ (Unit\,\mu L^{-1})}. \tag{B.1}$$

For a volumetric activity U ($units\cdot\mu\mathrm{L}^{-1}$) and a transcript of N_{all} nucleotides,

$$V_{\mathrm{unit}} = \frac{U}{N_{\mathrm{all}}}\,F_{\mathrm{Unit}}. \tag{B.2}$$

To relate Units to moles of active enzyme, we use the supplier's molar specific activity S_{mol} units$\cdot\,\mathrm{mol}^{-1}$); the active enzyme concentration is

$$E = \frac{U\,(10^6\ \mu\mathrm{L\,L^{-1}})}{S_{\mathrm{mol}}} \qquad (\mathrm{mol\,L^{-1}}). \tag{B.3}$$

With initiation dwell $\tau_{\mathrm{init}} = \ell_{\mathrm{init}}/v_{\mathrm{init}}$ and elongation speed v_{el} (nt min^{-1}),

$$r_{\mathrm{RNAP}} = \min\left\{\frac{1}{\tau_{\mathrm{init}}},\, \frac{v_{\mathrm{el}}}{N_{\mathrm{all}}}\right\}, \qquad V_{\mathrm{part}} = E\,r_{\mathrm{RNAP}}. \tag{B.4}$$

See Table D8 for parameter values.

Appendix C. dsRNA formation

During IVT, long dsRNA forms mostly by *intermolecular* pairing between the intended sense RNA and a small *antisense* complement that is co-produced. Once both are present, ions screen backbone charge and favor duplex growth; melting and strand exchange oppose it. We therefore model dsRNA as driven mainly by sense-antisense pairing. *Intramolecular* fold-backs (hairpins) are handled implicitly by an accessibility factor α that shrinks the fraction of each strand available to pair, and by a lumped loss rate k_{loss} that collects unzipping and exchange back to single strands.

We represent ion effects with a dimensionless screening factor

$$\Theta \;=\; 1 - \exp\!\big(-a\,[\mathrm{Mg}]_{\mathrm{free}} \;-\; a\,w_{\mathrm{spd}}\,[\mathrm{Spd}^{3+}]\big), \tag{C.1}$$

where $a > 0$ maps ionic dose to screening and $w_{\mathrm{spd}} > 1$ is a fixed weight for spermidine relative to Mg^{2+}. Thus both free Mg^{2+} and spermidine independently increase Θ toward a common plateau $0 \le \Theta < 1$.

We write the accessible fraction as

$$\alpha \;=\; \alpha_{\max}\big(1 - e^{-N_{\mathrm{all}}/N_0}\big)\,(1-\phi_{\mathrm{tail}})\,(1-\chi_\Theta\,\Theta), \tag{C.2}$$

$$\phi_{\mathrm{tail}} = \delta\,\min\!\left(1,\, \frac{N_{\mathrm{tail}}}{N^{*}_{\mathrm{tail}}}\right). \tag{C.3}$$

N_{all} is the resulting RNA length that can, in principle, take part in *inter*molecular pairing; N_0 sets how fast accessibility rises with length; $\alpha_{\max} \le 1$ is the long-length ceiling. The factor ϕ_{tail} removes non-pairing segments (the 3′ tail) using a maximum fractional penalty $\delta \in [0,1]$ and a saturation length N^{*}_{tail}. The term $(1-\chi_\Theta\,\Theta)$ captures that stronger screening stabilizes *intra*molecular hairpins and reduces intermolecular accessibility. All dsRNA parameters are found in Table D9

Intermolecular build-up and decay are:

$$V_{\mathrm{ann}} = \gamma\,\Theta\,\big(\alpha\,[\mathrm{RNA}]\big)^2, \tag{C.4}$$
$$V_{\mathrm{melt}} = k_{\mathrm{loss}}\,[\mathrm{dsRNA}], \tag{C.5}$$

with V_{ann} an effective second-order annealing flux for sense-antisense encounters and V_{melt} a first-order loss. The parameter $\gamma = \varepsilon_{\mathrm{as}}k_{\mathrm{on}}$ lumps antisense co-production and encounter/zipper rate. To reflect greater duplex stability at higher screening and for longer effective duplex length N_{all}, we take

$$k_{\mathrm{loss}} \;=\; k_0\,\exp(-\lambda_\Theta\,\Theta)\,\exp(-\lambda_L\,N_{all}) \tag{C.6}$$

- Increasing free Mg^{2+} or adding spermidine $\uparrow\,\Theta \Rightarrow$ faster productive encounters
- Increasing total NTP at fixed total Mg lowers $[\mathrm{Mg}]_{\mathrm{free}} \Rightarrow\downarrow\,\Theta$.
- Increasing T7 RNAP or DNA template raises the single-strand pool [RNA] and, via γ in (C.4).

Appendix D. Supplementary Tables

Table D.2
Parameter bounds for kinetic parameters sensitivity analysis

Parameter	Bounds	
$k_{app}\ (mM^{-1}s^{-1})$	0.001	0.0015
$k_1\ (mM^{-1})$	1.6	2.4
$k_2\ (mM^{-1})$	24	40
$k_{\mathrm{precip}}\ (mM^{-1})$	4	6
$k_{\mathrm{PPase}}\ (mM)$	2500	3750

Table D.3
Model variable bounds for sensitivity analysis

Parameter	Bounds
NTP (mM)	5 – 100
Magnesium (mM)	5 – 100
T7RNAP ($unit \cdot \mu L^{-1}$)	50 – 500
Spermidine (mM)	1 – 4
Template DNA (nM)	10 – 100
Time (Minutes)	10 – 240

Table D.4
Unit prices, reported in the same units as the model variables (1 L basis). Concentration-based inputs are in USD/(mM·L). Activity-dosed enzymes are in USD/kU. Template DNA is in USD/(nM·L) and is template-dependent.

Component (decision variable)	Unit price	Model unit / note
Total NTP (equimolar A/C/G/U)	451.01	USD/(mM·L)
T7RNAP	68.05	USD/kU
Template DNA (eGFP / CSP)	72.24 / 310.95	USD/(nM·L)
PPase	82.85	USD/kU
RNase inhibitor	0.0426	USD/kU
$MgCl_2$	0.00295	USD/(mM·L)
HEPES	0.176	USD/(mM·L)
TRIS-HCl	0.142	USD/(mM·L)
DTT	0.926	USD/(mM·L)
Spermidine	1.22	USD/(mM·L)
Gu-HCl	0.000205	USD/(mM·L)

Table D.5
Parameter bounds for CSP and eGFP template DNA LHS experiments

Parameter	Lower Bound	Upper Bound
Total NTP (mM)	4	60
Magnesium (mM)	5	90
T7RNAP ($unit \cdot \mu L^{-1}$)	100	400
Spermidine (mM)	1	4
Template DNA (nM)	20	100
Time (Minutes)	15	240

Table D.6
Parameters for precipitation experiments

Parameter	Amount / Range
Total NTP (mM)	40
Magnesium (mM)	8 - 80
T7RNAP (unit uL^{-1})	330
Spermidine (mM)	3
Template DNA (nM)	50
Time (Minutes)	120

Table D.7
Nucleotide composition of CSP and eGFP templates, including promoter-proximal transcribed region composition downstream of the T7 promoter.

Metric	CSP	eGFP
Full transcript nucleotide counts		
Adenine (A)	1106	266
Guanine (G)	1061	243
Cytosine (C)	1315	279
Uracil (U)	801	207
Total (nt)	**4283**	**995**
Promoter-proximal transcribed region (downstream of T7 promoter)		
Window length (nt)	53	47
Adenine (A)	17	27
Guanine (G)	9	12
Cytosine (C)	17	4
Uracil (U)	10	4
GC content (%)	49.06	34.04

Table D.8
Adopted equilibrium constants

K_i	$\log_{10} K$	T (°C)	Source	Notes
K_1	−4.42	25	[1]	-
K_2	−1.69	25	[1]	-
K_3	−1.49	25	[1]	-
K_4	−6.95	25	[1]	-
K_5	−8.94	25	[1]	-
K_6	−6.13	25	[1]	-
K_7	−3.05	25	[1]	-
K_8	−5.42	25	[1]	-
K_9	−2.33	25	[1]	-
K_{10}	−7.31	37	[2]	HEPES pK_a at 37 °C.
K_{11}	≈ −8.32	25	[3]	T7 RNAP-promoter ($K_d \approx 4.8$ nM); use as prior, fit at 37 °C/ionic strength.
K_{12}	110	37	[4, 5]	DNA-T7-spermidine effective coupling[a].
K_{13}	*Note* [a]	37	[4]	DNA-spermidine^{3+}; wide literature spread, treat as fitted[a].
K_{14}	*Note* [a]	37	[5]	T7 RNAP-spermidine^{3+}; include empirically, fit[a].
K_{15}	*not used*	25	[6]	Unrealistic for our system
K_{16}	−7.20	25	[6]	-.
K_{17}	−2.15	25	[6]	-
K_{18}	−2.87	25	[6]	$MgHPi^0$: WATEQ4F lists $\log_{10}\beta = 2.87$ (formation); here $\log_{10} K = -2.87$ (association)[b].
K_{19}	−4.756	25	[6]	Acetate pK_a baseline; small T-dependence.
K_{20}	−0.59	25	[7]	-
K_{21}	*not used*	25–37	[7]	Second acetate addition not detected within 0.1–0.5 M ($K_{21} \gg 0$.)

Notes. [a] Polyamine (spermidine^{3+}) interactions with DNA and proteins are highly sequence- and salt-dependent and often cooperative; treat K_{13}-K_{14} as lumped parameters represented completely as K_{12}.

Table D.9
Fixed parameters used for ceilings

Symbol	Meaning	Value	Units / note
U	T7 RNAP volumetric activity	330	$units \cdot \mu L^{-1}$
F_{Unit}	Unit→rate factor (Eq. (B1))	1.667×10^{-5}	mol L^{-1} min^{-1} per ($units \cdot \mu L^{-1}$)
E	Active RNAP (from Eq. (B3))	13.33	μM
ℓ_{init}	Initiation segment	8	nt
v_{init}	Initiation speed	0.5	nt s^{-1}
τ_{init}	Initiation dwell	16	s ($\ell_{\mathrm{init}}/v_{\mathrm{init}}$)
v_{el}	Elongation speed	200	nt s^{-1} (= 12,000 nt min^{-1})

Sources: 8, 9

Table D.10
Parameters for the dsRNA equations. “EO” denotes a heuristic influenced by literature based on CSP.

Symbol	Value	Basis
a	0.03 (0.02–0.05)	EO prior for ionic screening slope; consistent with ion-driven stabilization of RNA structures [10].
w_{spd}	12	EO prior for spermidine^{3+} potency relative to Mg^{2+}; polyamines and divalents both promote folding [10].
$\alpha_{\max}$	0.8 (0.6–1.0)	Cap on intermolecular accessibility; accessibility/opening vs. hybridization decomposition [11].
N_0	200 (100–300)	Length scale for accessibility rise; accessibility heuristics as in RNA:RNA binding models [11].
δ	0.5 (0.2–0.8)	Maximum tail penalty; EO within accessibility-based decompositions [11].
N^*_{tail}	50 (30–100)	Tail penalty saturation length; EO consistent with diminishing penalty beyond a characteristic length [11].
χ_Θ	0.2 (0.1–0.3)	Small salt-induced hairpin penalty; ions modulate loop/tertiary stability [10].
k_0	0.02 (0.01–0.05)	Baseline melt/branch-migration rate at low screening; nucleic-acid displacement kinetics literature [12, 13].
λ_Θ	2.5 (1–4)	Suppression of melt by screening; stronger ionic stabilization slows effective melting [10].
λ_L	0.002 (0.001–0.004)	Length-suppressed displacement/migration; rates decrease with longer exchange domains [12, 13].
γ	**Fit**	Heuristically set to give meaningful amount of dsRNA formation.

SI References

[1] D. Berg, Z. Kis, C.F. Behmer, K. Samnuan, A.K. Blakney, C. Kontoravdi, R. Shattock, N. Shah, Quality by design modelling to support rapid rna vaccine production against emerging infectious diseases. npj Vaccines 2021 6:1 6, 1–10 (2021) https://doi.org/10.1038/s41541-021-00322-7

[2] KGaA. Merck, Buffer Reference Center. Sigma-Aldrich. Web page; Sigma-Aldrich brand operated by Merck KGaA. https://www.sigmaaldrich.com/GB/en/technical-documents/protocol/protein-biology/ protein-concentration-and-buffer-exchange/buffer-reference-center Accessed 2025-09-08.

[3] A. Ujvári, C.T. Martin, Thermodynamic and kinetic measurements of promoter binding by t7 rna polymerase. Biochemistry 35(46), 14574–14582 (1996) https://doi.org/10.1021/bi961165g

[4] H. Deng, V.A. Bloomfield, J.M. Benevides, G.J.T. Jr, Structural basis of polyamine-dna recognition: spermidine and spermine interactions with genomic b-dnas of different gc content probed by raman spectroscopy. Nucleic acids research 28(17), 3379–3385 (2000).

[5] Z.J. Kartje, P. White, M. Brown, V. Gopalan, Revisiting t7 rna polymerase transcription in vitro with the comprehensive physiological buffer system. Nucleic Acids Research 48(6), 29 (2020) https://doi.org/10.1093/nar/gkz1162

[6] J.W. Ball, D.K. Nordstrom, User's manual for WATEQ4F, with revised ther modynamic data base and text cases for calculating speciation of major, trace, and redox elements in natural waters (1991).

[7] B. Hacht, Complex formation of acetic acid with ca(ii) and mg(ii) under physiological conditions. Journal of Solution Chemistry 37(2), 155–163 (2008) https://doi.org/10.1007/s10953-007-9233-3. Reports ML and ML_2 ($MgAc+, Mg(Ac)_2(aq)$) stability constants at 37 °C and I = 0.15 M NaCl.

[8] G.-Q. Tang, R. Roy, R.P. Bandwar, T. Ha, S.S. Patel, Real-time observation of the transition from transcription initiation to elongation of the rna polymerase. Proceedings of the National Academy of Sciences 106(52), 22175–22180 (2009) https://doi.org/10.1073/pnas.0906979106

[9] New England Biolabs: T7 RNA Polymerase (M0251). https://www.neb.com/en-us/products/m0251-t7-rna-polymerase Accessed 2025-09-12.

[10] D.E. Draper, Rna folding: thermodynamic and molecular descriptions of the roles of ions. Biophysical Journal 95(12), 5489–5495 (2008) https://doi.org/10.1529/biophysj.108.131813

[11] U. Mückstein, H. Tafer, J. Hackermüller, S.H. Bernhart, P.F. Stadler, I.L. Hofacker, Thermodynamics of rna-rna binding. Bioinformatics 22(10), 1177–1182 (2006) https://doi.org/10.1093/bioinformatics/btl024

[12] D.Y. Zhang, E. Winfree, Control of dna strand displacement kinetics using toe977 hold exchange. Journal of the American Chemical Society 131(47), 17303–17314 (2009) https://doi.org/10.1021/ja906987s

[13] P. Šulc, T.E. Ouldridge, F. Romano, J.P.K. Doye, A.A. Louis, Modelling toehold-mediated rna strand displacement. Biophysical Journal 108(5), 1238–1247 (2015) https://doi.org/10.1016/j.bpj.2015.01.023

References

[1] R.B. Kennedy, I.G. Ovsyannikova, P. Palese, G.A. Poland, Current challenges in vaccinology, Front. Immunol. 11 (2020) 1181. https://doi.org/10.3389/FIMMU.2020.01181

[2] N. Pardi, M.J. Hogan, F.W. Porter, D. Weissman, mRNA vaccines - a new era in vaccinology, Nature Rev. Drug Discovery 17 (2018) 261–279.

[3] S.S. Rosa, D.M. Prazeres, A.M. Azevedo, M.P. Marques, mRNA vaccine manufacturing: challenges and bottlenecks, Vaccine 39 (2021) 2190–2197.

[4] U. Sahin, K. Karikó, Ö. Türeci, mRNA-based therapeutics–developing a new class of drugs, Nat. Rev. Drug Discovery 13 (2014) 759–780. https://www.nature.com/articles/nrd4278.

[5] A. Schmidt, H. Helgers, F.L. Vetter, S. Zobel-Roos, A. Hengelbrock, J. Strube, Process automation and control strategy by quality-by-Design in total continuous mRNA manufacturing platforms, Processes 10 (9) (2022). https://doi.org/10.3390/pr10091783

[6] S. Daniel, Z. Kis, C. Kontoravdi, N. Shah, Quality by design for enabling RNA platform production processes, Trends Biotechnol. (2022). https://www.cell.com/trends/biotechnology/fulltext/S0167-7799(22)00080-4.

[7] A. Nair, Z. Kis, Bacteriophage RNA polymerases: catalysts for mRNA vaccines and therapeutics manufacturing, Front. Mol. Biosci. 11 (2024) . https://doi.org/10.3389/fmolb.2024.1504876

[8] D. van de Berg, Z. Kis, C.F. Behmer, K. Samnuan, A.K. Blakney, C. Kontoravdi, R. Shattock, N. Shah, Quality by design modelling to support rapid RNA vaccine production against emerging infectious diseases, npj Vaccines 2021 6:1 6 (2021) 1–10. https://doi.org/10.1038/s41541-021-00322-7

[9] N.M. Stover, K. Ganko, R.D. Braatz, Mechanistic modeling of in vitro transcription incorporating effects of magnesium pyrophosphate crystallization, Biotechnol. Bioeng. 121 (9) (2024) 2636–2647.

[10] K. Samnuan, A.K. Blakney, P.F. McKay, R.J. Shattock, Design-of-experiments in vitro transcription yield optimization of self-amplifying RNA, BioRxiv (2021) 2021–01.

[11] J. Boman, T. Marušič, T.V. Seravalli, J. Skok, F. Pettersson, K.Š. Nemec, H. Widmark, R. Sekirnik, Quality by design approach to improve quality and decrease cost of in vitro transcription of mRNA using design of experiments, Biotechnol. Bioeng. 121 (11) (2024) 3415–3427.

[12] F.L. Vetter, S. Zobel-Roos, J. Mota, B. Nilsson, et al., Toward autonomous production of mRNA-therapeutics in the light of advanced process control and traditional control strategies for chromatography, Processes 10 (9) (2022) 1868. https://doi.org/10.3390/pr10091868

[13] J. Gilman, L. Walls, L. Bandiera, et al., Statistical design of experiments for synthetic biology, ACS Synth. Biol. 10 (1) (2021) 1–10. https://doi.org/10.1021/acssynbio.0c00385

[14] R. Kumar, N. Le, Z. Tan, M.E. Brown, S. Jiang, et al., Efficient polymer-mediated delivery of gene-editing ribonucleoprotein payloads through combinatorial design, parallelized experimentation, and machine learning, ACS Nano 14 (11) (2020) 14294–14307. https://doi.org/10.1021/acsnano.0c08549

[15] S. Akama, M. Yamamura, T. Kigawa, A multiphysics model of in vitro transcription coupling enzymatic reaction and precipitation formation, Biophys. J. 102 (2012) 221–30. https://doi.org/10.1016/j.bpj.2011.12.014

[16] M.C. Hohnholt, R. Dringen, Spermidine influences DNA and RNA synthesis in the brain, Neurochem. Int. 61 (4) (2012) 702–708.

[17] N.J. Kuhn, S. Ward, Purification, properties, and multiple forms of a manganese-Activated inorganic pyrophosphatase from bacillus subtilis, Arch. Biochem. Biophys. 1998 (1998). https://doi.org/10.1016/S0003-9861(98)90629-4

[18] C. Andersson, C. Führer, J. Åkesson, Assimulo: a unified framework for {ODE} solvers, Math. Comput. Simul. 116 (0) (2015) 26–43. https://doi.org/http://dx.doi.org/10.1016/j.matcom.2015.04.007

[19] E.N. Welbourne, K.A. Loveday, A. Nair, E. Nourafkan, J. Qu, K. Cook, Z. Kis, M.J. Dickman, Anion exchange HPLC monitoring of mRNA in vitro transcription reactions to support mRNA manufacturing process development, Front. Mol. Biosci. 11 (2024). https://doi.org/10.3389/fmolb.2024.1250833

[20] P. Virtanen, R. Gommers, T.E. Oliphant, M. Haberland, T. Reddy, D. Cournapeau, E. Burovski, P. Peterson, W. Weckesser, J. Bright, S.J. van der Walt, M. Brett, J. Wilson, K.J. Millman, N. Mayorov, A.R.J. Nelson, E. Jones, R. Kern, E. Larson, C.J. Carey, İ. Polat, Y. Feng, E.W. Moore, J. VanderPlas, D. Laxalde, J. Perktold, R. Cimrman, I. Henriksen, E.A. Quintero, C.R. Harris, A.M. Archibald, A.H. Ribeiro, F. Pedregosa, P. van Mulbregt, SciPy 1.0 Contributors, Scipy 1.0: fundamental algorithms for scientific computing in python, Nat. Methods 17 (2020) 261–272. https://doi.org/10.1038/s41592-019-0686-2

[21] J. Herman, W. Usher, SALib: An open-source python library for sensitivity analysis, The J. Open Source Softw. 2 (9) (2017). https://doi.org/10.21105/joss.00097

[22] Z. Kis, C. Kontoravdi, R. Shattock, N. Shah, Resources, production scales and time required for producing RNA vaccines for the global pandemic demand, Vaccines 9 (1) (2021). https://doi.org/10.3390/vaccines9010003

[23] P. Thomen, P.J. Lopez, U. Bockelmann, J. Guillerez, M. Dreyfus, F. Heslot, T7 RNA Polymerase studied by force measurements varying cofactor concentration, Biophys. J. 95 (5) (2008) 2423–2433. https://doi.org/10.1529/BIOPHYSJ.107.125096

[24] D. Temiakov, V. Patlan, M. Anikin, W.T. McAllister, S. Yokoyama, D.G. Vassylyev, Structural basis for substrate selection by T7 RNA polymerase, Cell 116 (3) (2004) 381–391. https://doi.org/10.1016/S0092-8674(04)00059-5

[25] Y.W. Yin, T.A. Steitz, Structural basis for the transition from initiation to elongation transcription in T7 RNA polymerase, Science 298 (5597) (2002) 1387–1395. https://doi.org/10.1126/science.1077464

[26] H.R. Koh, R. Roy, M. Sorokina, G.Q. Tang, D. Nandakumar, S.S. Patel, T. Ha, Correlating transcription initiation and conformational changes by a single-subunit RNA polymerase with near base-pair resolution, Mol. Cell 70 (5) (2018) 695–706. https://doi.org/10.1016/J.MOLCEL.2018.04.018

[27] Y. Sari, S. Sousa Rosa, J. Jeffries, M.P.C. Marques, Comprehensive evaluation of T7 promoter for enhanced yield and quality in mRNA production, Sci. Rep. 14 (1) (2024) 9655. https://doi.org/10.1038/s41598-024-59978-5

[28] Y.W. Yin, T.A. Steitz, The structural mechanism of translocation and helicase activity in T7 RNA polymerase, Cell 116 (3) (2004) 393–404. https://doi.org/10.1016/S0092-8674(04)00120-5

[29] N.M. Stover, S. Ahmadi, J. Rosenfeld, F. Destro, A.S. Myerson, R.D. Braatz, Model-Based optimization of fed-Batch in vitro transcription, Chembiochem 26 (21) (2025) e202500485. https://doi.org/https://doi.org/10.1002/cbic.202500485
[30] J. Skok, P. Megušar, T. Vodopivec, D. Pregeljc, N. Mencin, M. Korenč, A. Krušič, A.M. Celjar, N. Pavlin, J. Krušič, M. Mueller, K. McHugh, A. Štrancar, R. Sekirnik, Gram-Scale mRNA production using a 250-ml single-Use bioreactor, Chem. Ing. Tech. 94 (12) (2022) 1928–1935. https://doi.org/https://doi.org/10.1002/cite.202200133
[31] L. Guo, Z. Liu, S. Song, W. Yao, M. Yang, G. Chen, Maximizing the mRNA productivity for in vitro transcription by optimization of fed-batch strategy, Biochem. Eng. J. 210 (2024) 109412. https://doi.org/https://doi.org/10.1016/j.bej.2024.109412